The Journal of Navigation (2022), **75**:3 554–571
doi:10.1017/S0373463322000078

CAMBRIDGE UNIVERSITY PRESS

RESEARCH ARTICLE

H_i/H_∞-optimised fault detection for a surface vessel integrated navigation system

Muzhuang Guo,[1] Chen Guo,[1]* and Chuang Zhang[2]

[1] College of Marine Electrical Engineering, Dalian Maritime University, Dalian, Liaoning, China
[2] Navigation College, Dalian Maritime University, Dalian, Liaoning, China.
*Corresponding author. E-mail: dmuguoc@126.com

Received: 20 April 2021; **Accepted:** 03 October 2021; **First published online:** 25 March 2022

Keywords: fault detection; surface vessel integrated navigation; H_i/H_∞ optimisation; fault detection filter; threshold

Abstract

Strapdown inertial navigation systems are widely used in surface ships and warships. Although high-precision optical fibre inertial navigation systems are available, they have high cost and limited practicality. Therefore, they cannot replace the traditional platform inertial navigation systems in all ships. Hence, microelectromechanical system (MEMS)-based inertial sensors are widely used for robust navigation. Accurate and timely identification of sensor faults while ensuring stable navigation is a challenging task. This paper proposes a robust fault detection (FD) approach for a low-cost system that loosely integrates a strapdown inertial navigation system and the global navigation satellite system, where the integrated navigation state estimation provides high-accuracy output. A cubature H_i/H_∞-optimised FD filter was designed for a nonlinear discrete time-varying system considering sensitivity to faults and robustness to disturbances. Furthermore, a threshold for FD was derived considering a compromise between the false alarm rate and fault diagnosis accuracy. Finally, the proposed method was validated through simulations using multiple noise distribution sensor data generated by a ship-manoeuvring simulator.

1. Introduction

Autonomous marine underwater or unmanned surface vessels have been widely used in various fields, such as marine administration and resource exploration (Qin et al., 2019; Wang et al., 2019; Liu et al., 2020; Wang et al., 2020). The type of engineering involved therein relies on the stable transmission of sensor signals and real-time feedback. To regulate the equipment of ships, particular regulations and operation specifications are designed for different fields. In addition, the standards of the navigation sensors are based on conventions adopted by the International Maritime Organization or regulations formulated by organisations such as the Institute of Electrical and Electronics Engineers (IEEE), Institution of Engineering and Technology (IET), and Det Norske Veritas (IEEE, 2008; IMO, 2009).

In practical applications, however, navigation sensors have their own limitations. Moreover, additional standby signals are often required to ensure navigation safety. An inertial navigation system can determine the attitude, position, and velocity information of a vessel independently (without depending on the outside world) using the integration principle. Because of being independent, a strapdown inertial navigation system (SINS) can be used as redundant equipment to ensure the safety of navigation. However, the motion state provided by the SINS alone, which is widely adopted in ships, degrades with time owing to its working principle. High-precision navigation sensors, such as laser/fibre-optic gyroscopes, can be used in all types of surface vessels. However, their cost and practicality cannot compete with those of the traditional platform navigation systems in all ships, especially

© The Author(s), 2022. Published by Cambridge University Press on behalf of The Royal Institute of Navigation

https://doi.org/10.1017/S0373463322000078 Published online by Cambridge University Press

in ships that are already equipped with a platform gyrocompass. The global navigation satellite system (GNSS) can provide long-term and accurate position and velocity of the ship (Liu et al., 2021). However, GNSS data suffer from signal interruption and outliers. To overcome these shortcomings, a SINS/GNSS integrated navigation system has been explored (Majidi et al., 2020; Xiong et al., 2020). Previous works on algorithms for integrated navigation considered the use of the statistical Kalman filter (KF), extended Kalman filter (EKF), unscented Kalman filter (UKF), cubature Kalman filter (CKF) and other methods (Liu et al., 2019b; Chiang et al., 2020; Li et al., 2020; Song et al., 2020). Among these methods, the performance of CKF is similar to that of UKF with less computational cost than UKF and particle filter. With regard to navigation sensors, high-precision navigation sensors, such as laser/fibre-optic gyroscopes, are commonly used in large warships, whereas microelectromechanical system (MEMS) sensors are used more widely despite their comparatively poor accuracy and reliability. In a MEMS SINS/GNSS system, factors such as temperature and electromagnetic interference often seriously affect the sensor characteristics. Designing a fault detection (FD) method with robustness to modelling error, sensitivity to faults and high-precision estimation outputs of the motion state is a difficult task in integrated navigation systems. FDs for the SINS/GNSS integrated navigation system have received increased research attention as a solution to this problem.

There are two main types of FD algorithms for the SINS/GNSS system: (1) FD and isolation based on a neural network (NN) (Guo et al., 2018, 2020; Xu and Lian, 2018; Zhu and Zhou, 2020) and (2) a statistical algorithm based on the chi-square test, time and frequency domain features (Jiang et al., 2019; Zhao et al., 2019; Gao et al., 2020; Xiong et al., 2020; Zhang et al., 2020). For FD based on NN (Guo et al., 2020) an approach for fault-tolerant integrated navigation post fault diagnosis has been proposed. Further, a multichannel one-dimensional fully convolutional NN (CNN) FD method was proposed to extract the fault features with various scales (Guo et al., 2018; Xu and Lian, 2018). Machine learning was used to estimate state variance to construct the test statistic, which was used for the chi-square test FD (Zhu and Zhou, 2020). However, the high computational burden of the CNN and the need for sufficient learning samples directly affect the performance of real-time detection. The most commonly used residual chi-square test is considerably simpler. An FD method that simultaneously detects measurement outliers and the statistical characteristics of measurement noise was proposed (Zhu and Zhou, 2020). Further, two appropriate thresholds were set to reduce the influence of the undetected measurement in FD (Xiong et al., 2020). However, none of these methods sufficiently consider the condition where statistical properties are unavailable without substantial empirical data. Thus, noise and faults are difficult to define. Among the many significant results in this regard, an H_i/H_∞ observer-based FD filter (FDF) (Zhong et al., 2010, 2015, 2016) was proposed considering not only the sensitivity to faults but also robustness to disturbances. In the framework of the so-called H_-/H_∞ optimisation FDF, the H_∞ norm is defined as the robustness index to an unknown input, and H_- is defined as the sensitivity index of faults towards the residual (Wang et al., 2007). The H_i/H_∞ optimisation based on this framework has been widely studied for linear discrete time-varying (LDTV) systems (Li and Zhou, 2009; Khan et al., 2014). More recently, for nonlinear systems, an extended H_i/H_∞ FDF was proposed by Zhong et al. (2015) with a corresponding postfilter; this system has been used in various fields (Zhong et al., 2019; Liu et al., 2018) to analyse the fault diagnosis performance of satellite attitude control systems with process disturbances and measurement noise.

However, the observer-based extended H_i/H_∞ FDF highly relies on the linear Jacobian transformation matrix of systems. When dealing with a strong nonlinear system, the FD results are degraded by the interference error. In such an event, the system cannot provide a stable output, thereby rendering the fault diagnosis results meaningless. In this work, the surface vessel MEMS SINS/GNSS integrated system is considered to explore a solution for the problem of unstable output of the FDF. For this purpose, a cubature H_i/H_∞ FD method with l_2-norm bounded unknown inputs and energy-bounded process disturbance and measurement noise is proposed here.

The rest of this paper is organised as follows. Section 2 provides a brief introduction of the ship SINS/GNSS system and the FDF for an LDTV system. In Section 3, a cubature H_i/H_∞ FDF considering

https://doi.org/10.1017/S0373463322000078 Published online by Cambridge University Press

a false alarm rate (FAR) is proposed. Section 4 describes a simulation based on a ship-manoeuvring simulator that is performed to verify the effectiveness of the proposed FD method and compares the performances of the proposed FD method with that of a previously developed extended H_i/H_∞ FDF. Finally, the conclusions are given in Section 5.

2. Preliminaries and problem statement

This section first introduces the principle of the GNSS/SINS system in a ship. Then, considering the complex natural environment and frequent disturbances encountered by ships sailing at sea, a widely used singular value decomposition (SVD) CKF with high numerical stability under multiple iterations is introduced. Moreover, the H_i/H_∞ FDF in an LDTV system is reviewed.

2.1. Dynamic model of the ship SINS/GNSS system

Following the report by Liang and Jia (2015), the frame origin at the centroid of the ship, navigation frame, and Earth-centred frame are denoted as b, n and e, respectively. The i frame denotes the Earth-fixed frame, and the n' frame denotes the frame computed by SINS relative to the true navigation frame. C_B^A denotes the rotation matrix between A and B. ω_{AB}^C denotes the rotational rate along C with respect to A or B. Thus, we obtain the nonlinear error model states:

$$\begin{aligned}
\delta\dot{\Omega} &= (I - C_n^{n'})\omega_{in}^n + \delta\omega_{in}^n + C_b^{n'}\varepsilon \\
\delta\dot{V} &= [I - (C_n^{n'})]C_b^n\hat{f}^b - (2\delta\omega_{ie}^n + \delta\omega_{en}^n) \times (\hat{V} - \delta V) + \delta g + C_b^{n'}\nabla \\
\delta\dot{P} &= \delta V + [-\dot{L}, \dot{\lambda}\cos L, -\dot{\lambda}\sin L]\delta P,
\end{aligned} \tag{1}$$

where $\delta\dot{\Omega}, \delta\dot{V}$, and $\delta\dot{P}$ denote the component error vectors of attitude, velocity and position, respectively, in the navigation frame, and g represents the gravitational acceleration. ε and ∇ denote the constant gyroscope bias vector and accelerometer bias vector L and λ denote the latitude and longitude of the vehicle, respectively. Moreover, f^b and ω_{ib}^b denote the output of the accelerometer and the gyro in the b frame, respectively. In addition, considering that the speed of the ship is much smaller than the speed of rotation of the Earth, the following equation is obtained (Wen et al., 2019):

$$\begin{aligned}
\delta\omega_{ie}^n &= [0, -\omega_{ie}\sin\hat{L}\delta L, \omega_{ie}\cos\hat{L}\delta L] \\
\delta\omega_{en}^n &= [-\delta V_N/(R_e(1 - 2e + 3e\sin L^2) + \hat{h}), \delta\dot{\lambda}\cos\hat{L} - \lambda\cos\hat{L}\delta L, \\
&\qquad \delta\dot{\lambda}\sin\hat{L} + \lambda\cos\hat{L}\delta L].
\end{aligned} \tag{2}$$

where R_e is the length if the semimajor axis of the ellipsoid.

The SINS/GNSS integrated system of the surface vessel can then be described as follows:

$$\begin{aligned}
x_k &= \ell_k(x_{k-1}) + B_k\omega_{k-1} + B_f f_{k-1} \\
z_k &= C_k x_{k-1} + D_k v_k + D_f f_k,
\end{aligned} \tag{3}$$

where x_k and z_k denote the state and measurement vectors in the kth epoch, respectively. The noise of SINS ω_k and that of GNSS v_k are uncertain and stochastic. When sensor faults exist, the progress and measurement faults are denoted as f_{1k} and f_{2k}, respectively. In addition, $f_k = [f_{1,k}, f_{2,k}]^{\mathrm{T}}$. ℓ_k is the state transition function.B_k, C_b^n and C_k represent known matrices comprising module matrices. $B_f = [B_k, 0]^{\mathrm{T}}.D_k = D_f = [0, I]^{\mathrm{T}}$.

https://doi.org/10.1017/S0373463322000078 Published online by Cambridge University Press

2.2. H_i/H_∞ FDF for LDTV system

An LDTV system can be described using the same notations as those in Equation (3):

$$\begin{aligned} x_k &= F_{l,k}x_{k-1} + B_{l,k}\omega_{k-1} + B_{lf,k}f_{k-1} \\ z_k &= C_{l,k}x_{k-1} + D_{l,k}v_k + D_{lf,k}f_k \end{aligned} \tag{4}$$

Here, Equation (4) differs from (3) in that the known $F_{l,k}$, $B_{l,k}$, $B_{lf,k}$ and $C_{l,k}$, $D_{l,k}$, $D_{lf,k}$ are the linearised matrices of input, noise and fault with appropriate dimensions. To detect faults in Equation (4), one can use a residual observer-based FD system, also known as an FDF (Liu et al., 2018, 2019a), for residual generation, which is an important task of FD. When $(C_{l,k}, F_{l,k})$ is detectable and $(F_{l,k}, B_{l,k})$ is uniformly stabilisable, the following general residual r_k observer-based FDF is proposed:

$$\begin{cases} \hat{x}_k = F_{l,k}\hat{x}_{k-1} + L_{k-1}\tilde{y}_{k-1} \\ \tilde{y}_k = z_k - C_{l,k}\hat{x}_k \\ r_k = W_k\tilde{y}_k \end{cases} \tag{5}$$

Let $e_k = x_k - \hat{x}_k$. From Equations (4) and (5),

$$\begin{cases} e_k = (F_{l,k} - L_kC_{l,k})e_{k-1} + (B_{l,k}w_k - L_kD_{l,k}v_k) \\ \qquad + (B_{lf,k} - L_kD_{lf,k})f_k \\ \tilde{y}_k = C_{l,k}e_k + D_{l,k}v_k + D_{lf,k}f_k \\ r_k = W_k\tilde{y}_k \end{cases} \tag{6}$$

where L_k is the observer gain matrix of the observation and W_k denotes the postfilter matrix.

The transition matrix is defined as $\phi_{k|i} = \prod_{j=i}^{k-1}(F_{l,k|j} - L_jC_{l,k|j})$. Let $g_{d,k|i} = C_{l,k}\phi_{k|i+1}(B_{l,i} - L_kD_{l,i})$ and $g_{f,k|i} = C_{l,k}\phi_{k|i+1}(B_{l,i} - L_kD_{lf,i})$, where $g_{\varepsilon,k} = [C_k\phi_{k|0}, g_{d,k|0}, \ldots, g_{d,k|k-1}, D_{l,k}]$ and $g_{\varepsilon f,k} = [g_{f,k|0}, \ldots, g_{f,k|k-1}, D_{lf,k}]$. The residual generator then takes the form $r_k = r_{d,k} + r_{f,k}$, $r_{d,k} = W_kg_{\varepsilon,k}d_k$, $r_{f,k} = W_kg_{\varepsilon f,k}f_k$.

The following indices are defined considering the robustness of the indices to the unknown noise or inputs and sensitiveness to the faults:

$$\begin{aligned} ||G_{rd}||^2_{\infty,[0,N]} &= \sup_{f=0} \frac{\sum_{k=0}^{N}||r_{d,k}||^2}{x_0^{\mathrm{T}}\kappa_0^{-1}x_0 + \sum_{k=0}^{N}(||d_k||^2)} \\ ||G_{rf}||^2_{\infty,[0,N]} &= \sup_{x_0,\omega,v=0} \frac{\sum_{k=0}^{N}||r_{f,k}||^2}{\sum_{k=0}^{N}||f_k||^2} \\ ||G_{rf}||^2_{-,[0,N]} &= \inf_{x_0,\omega,v=0} \frac{\sum_{k=0}^{N}||r_{f,k}||^2}{\sum_{k=0}^{N}||f_k||^2} \end{aligned} \tag{7}$$

where $\kappa_0 = x_0x_0^{\mathrm{T}} = P_0$. $||G_{rd}||^2_{\infty,[0,N]}$ represents the index indicating the robustness of the residual to unknown inputs or acceptable noise. Further, for FD, $||G_{rf}||^2_{\infty,[0,N]}$ and $||G_{rf}||^2_{-,[0,N]}$ represent the sensitivities of r_k toward faults in the best- and worst-case scenarios, respectively.

Thus, the goal of r_k is to reduce the unknown input and simultaneously enhance the sensitivity to the faults. Thus, the following maximisation should be satisfied:

$$\max_{L_k,W_k} \frac{||G_{rf}||^2_{\infty,[0,N]}}{||G_{rd}||^2_{\infty,[0,N]}} \text{ or } \max_{L_k,W_k} \frac{||G_{rf}||^2_{-,[0,N]}}{||G_{rd}||^2_{\infty,[0,N]}}, \tag{8}$$

which is the so-called H_i/H_∞-FDF (Zhong et al., 2020).

https://doi.org/10.1017/S0373463322000078 Published online by Cambridge University Press

Let $r_{dk} = \text{col}\{r_{di}\}_{i=0}^{k}$, $r_{fk} = \text{col}\{r_{fi}\}_{i=0}^{k}$. We have $r_{dk} = H_{rd} d_k$ and $r_{kf} = H_{rf} f_k$. H_{rd} and H_{rf} are as follows:

$$H_{rd,k} = \begin{bmatrix} \bar{g}_{e,0|0} & \bar{D}_{l,0} & 0 & \cdots & \cdots & 0 \\ \bar{g}_{e,0|0} & \bar{g}_{d,1|0} & \bar{D}_{l,1} & 0 & \cdots & 0 \\ \vdots & \vdots & \vdots & \ddots & \ddots & 0 \\ \bar{g}_{e,k|0} & \bar{g}_{e,k|0} & \bar{g}_{e,k|1} & \cdots & \bar{g}_{e,k|k-1} & \bar{D}_{l,k} \end{bmatrix}$$
$$H_{rf,k} = \begin{bmatrix} \bar{D}_{lf,0} & 0 & \cdots & \cdots & 0 \\ \bar{g}_{f,1|0} & \bar{D}_{lf,1} & 0 & \cdots & 0 \\ \vdots & \ddots & \ddots & \ddots & 0 \\ \bar{g}_{f,k|0} & \bar{g}_{f,k|1} & \cdots & \bar{g}_{f,k|k-1} & \bar{D}_{lf,k} \end{bmatrix}, \tag{9}$$

where $\bar{g}_{e,i|0} = W_i g_{e,i|0}$, $\bar{g}_{e,i|j} = W_i g_{e,i|j}$, $\bar{D}_{l,i} = W_i D_{l,i}$, and $\bar{g}_{f,i|j} = W_i g_{f,i|j}$, $\bar{D}_{lf|i} = W_i D_{lf|i}$, $i \le k, j \le i-1$.

Then, we have $||G_{rd}||^2_{\infty,[0,N]} = ||H_{rd,k}||_2$, $||G_{rf}||^2_{\infty,[0,N]} = ||H_{rf,k}||_2$, and $||G_{rf}||^2_{-,[0,N]} = ||H_{rf}||_-$.

Based on the above definitions, Equation (8) can be rewritten as

$$\max_{L_k, W_k} \frac{||H_{rf}||_2}{||H_{rd}||_2} \text{ or } \max_{L_k, W_k} \frac{||H_{rf}||_-}{||H_{rd}||_2}. \tag{10}$$

At this juncture, note that $E\{||r_{dk}||\} \le ||H_{rd,k}|| \cdot E\{||d_k||\}$, $E\{||r_{fk}||\} \le ||H_{rf,k}||_2 \cdot E\{||f_k||\}$ and $E\{||r_{fk}||\} \ge ||H_{rf,k}||_- \cdot E\{||f_k||\}$. Thus, using Equation (4), H_i/H_∞ can be applied to an FD subject.

With regard to residual evaluation, considering the choice of the threshold, the following assumption is made:

$$x_0^{\mathrm{T}} \kappa_0^{-1} x_0 + \sum_{k=0}^{N} (\omega_k^{\mathrm{T}} \Theta^{-1} \omega_k + v_k^{\mathrm{T}} \Xi^{-1} v_k) \le \delta_d^2 \tag{11}$$

According to this inequality, the error introduced by the estimated initial value x_0, process noise ω_k and measurement noise v_k is less than or equal to the set threshold δ_d. Θ, Ξ and κ_0 are weighting matrices determined in the normal case of the above covariance matrix. However, choosing an analytical value of δ_d in real applications is very difficult. Generally, the value is selected based on historical data or experience.

When $J_N > J_{th,0}$ with an FAR of zero, the $l_2[0, N]$ norm-type evaluation J_N and threshold $J_{th,0}$ with a moderately set sliding window N can be selected as follows:

$$J_N = \frac{1}{N+1} \sum_{k=0}^{N} r_k^{\mathrm{T}} r_k$$
$$J_{th,0} = \frac{1}{N+1} ||G_{rd}||^2_{\infty,[0,N]} \delta_d^2 \tag{12}$$

3. Integrated disturbance compensation and cubature H_i/H_∞ FDF design

3.1. Derivation of the Krein space CKF

To address the nonlinearity in the FD problem using the H_i/H_∞ optimised method from Equation (3), a statistical linearisation approach was adopted.

Consider the nonlinear function of ℓ_k in Equation (3), evaluated for $i = 1, \ldots 2n$ sampling mapping $(\chi^i_{k-1|k-1}, \hat{x}^i_{k|k-1})$, where $\chi^i_{k|k-1} = \ell_k(\chi_{k-1|k-1})$, $\hat{x}_{k|k-1} = (1/2n) \sum_{i=1}^{2n} \chi^i_{k|k-1}$ (Julier et al., 2000).

https://doi.org/10.1017/S0373463322000078 Published online by Cambridge University Press

Assuming that the $\hat{x}^i_{k|k-1}$ can be statistically linearised as $\hat{x}_{k|k-1} = A(\chi^i_{k-1|k-1}) + b + \varsigma$, the object can be transformed to obtain $\hat{A}$ and $\hat{b}$ such that the pointwise linearisation error ς is minimised:

$$\{\hat{A}, \hat{b}\} = \arg\min \varsigma\varsigma^{\mathrm{T}} \tag{13}$$

where $\varsigma = (1/2n)\sum_{i=1}^{2n}(\hat{x}^i_{k|k-1} - (A\chi^i_{k-1|k-1} + b))$. Consider the derivatives of objective function with respect to A and b. Taking them to be zero gives the following:

$$\begin{aligned} \hat{b} &= \bar{x} - \hat{A}\bar{\chi} \\ \hat{A} &= (P^{x\chi}_{k|k-1})^{\mathrm{T}}(P^{xx}_{k-1|k-1})^{-1}, \end{aligned} \tag{14}$$

where the parameters are obtained as $\bar{\chi} = (1/2n)\sum_{i=1}^{2n}\chi^i_{k-1|k-1}$, $\bar{x} = (1/2n)\sum_{i=1}^{2n}x^i_{k|k-1}$; $P^{xx}_{k-1|k-1} = (1/2n)\sum_{i=1}^{2n}(\chi^i_{k-1|k-1} - \bar{\chi})(\chi^i_{k-1|k-1} - \bar{\chi})^{\mathrm{T}}$; and $P^{x\chi}_{k|k-1} = (1/2n)\sum_{i=1}^{2n}(\chi^i_{k-1|k-1} - \bar{\chi})(\hat{x}^i_{k|k-1} - \bar{x})^{\mathrm{T}}$. Then, the estimation error covariance can be calculated as

$$\begin{aligned} P_{\varsigma\varsigma} &= \hat{\varsigma}\hat{\varsigma}^{\mathrm{T}} \\ &= (1/2n)\sum_{i=1}^{2n}(\hat{x}^i_{k|k-1} - \bar{x} - \hat{A}(\chi^i_{k-1|k-1} - \bar{\chi}))\,(\hat{x}^i_{k|k-1} - \bar{x} - \hat{A}(\chi^i_{k-1|k-1} - \bar{\chi}))^{\mathrm{T}} \\ &= P^{xx}_{k|k-1} - \hat{A}P^{xx}_{k-1|k-1}\hat{A}^{\mathrm{T}} = P^{xx}_{k|k-1} - (P^{x\chi}_{k|k-1})(P^{xx}_{k-1|k-1})^{-1}(P^{x\chi}_{k|k-1}), \end{aligned} \tag{15}$$

where $P^{xx}_{k|k-1}$ denotes the covariance of $(\hat{x}^i_{k|k-1} - \bar{x})$.

Now, considering the exception and the outer product of the statistical linearised model, we obtain the posterior statistics given by

$$x_{k+1} = (P^{x\chi}_{k|k-1})^{\mathrm{T}}(P^{xx}_{k-1|k-1})^{-1}(x_k - \hat{x}_{k-1|k-1}) + \hat{x}_{k|k-1} + e_k + w_k. \tag{16}$$

The linearisation error e_k, obtained as $E(e_k e_k^{\mathrm{T}}) = P^{xx}_{k|k-1} - (P^{x\chi}_{k|k-1})^{\mathrm{T}}(P^{xx}_{k-1|k-1})^{-1}P^{x\chi}_{k|k-1}$, has a normal Gaussian distribution with zero mean (Zhao and Mili, 2019).

The same linearisation procedure can be used for the measurement function:

$$E(\tau_k\tau_k^{\mathrm{T}}) = P^{zz}_{k|k-1} - (P^{xz}_{k|k-1})^{\mathrm{T}}(P^{xx}_{k|k-1})^{-1}P^{xz}_{k|k-1}, \tag{17}$$

where τ_k, obtained as $E(\tau_k\tau_k^{\mathrm{T}}) = P^{zz}_{k|k-1} - (P^{xz}_{k|k-1})^{\mathrm{T}}(P^{xx}_{k|k-1})^{-1}P^{xz}_{k|k-1}$, has the same properties as e_k.

Thus, according to Equations (15) and (16), Equation (3) can be transformed as follows:

$$\begin{aligned} x_k &= F_{l,k}(x_{k-1} - \hat{x}_{k-1|k-1}) + \hat{x}_{k|k-1} + e_k + B_{l,k}w_k + B_{lf,k}f_k \\ z_k &= C_{l,k}(x_k - \hat{x}_{k|k-1}) + \hat{z}_{k|k-1} + \tau_k + D_{l,k}v_k + D_{lf,k}f_k, \end{aligned} \tag{18}$$

where $F_{l,k} = (P^{x\chi}_{k|k-1})^{\mathrm{T}}(P^{xx}_{k-1|k-1})^{-1}$, $C_{l,k} = (P^{xz}_{k|k-1})^{\mathrm{T}}(P^{xx}_{k|k-1})^{-1}$.

Remark 1: If we move $F_{l,k}\hat{x}_{k-1|k-1}$ and $\hat{x}_{k|k-1}$ to the left-hand side of Equation (18), which is more reasonable in the physical sense, $C_{l,k}\hat{x}_{k|k-1}$ and $\hat{z}_{k|k-1}$ are also moved to the left-hand side of the equation. However, this will suppress outlier detection because of data redundancy. For example, if the left side of the observation function is $z_k + C_{l,k}\hat{x}_{k|k-1} - \hat{z}_{k|k-1}$, the measurement error will be influenced by redundant process noise from the state estimation function and measurement noise as well as by outliers from the observation function, which leads to the equation being affected by noise and faults several times.

https://doi.org/10.1017/S0373463322000078 Published online by Cambridge University Press

3.1.1. Design of a nonlinear H_i/H_∞-FDF

As described in the previous sections, the CKF-integrated navigation system is linearised. Then, to solve the problem of Equation (8), an optimal L_k and W_k in the observer-based FDF are determined by applying the solution of the linearised H_i/H_∞-FDF in Zhong et al. (2010).

Thus, the following observer-based FDF of the system presented in Equation (18) was considered.

$$\begin{aligned} \hat{x}_k &= F_{l,k}\hat{x}_{k-1} + L_{k-1}\tilde{z}_{k-1} - F_{l,k}\hat{x}_{k-1|k-1} + \hat{x}_{k|k-1} + e_k \\ \tilde{z}_k &= z_k - C_{l,k}\hat{x}_k \\ r_k &= W_k\tilde{z}_k, \end{aligned} \tag{19}$$

where the residual function J_N and the FD logic are as given in Equation (12).

Next, the following terms are defined: $\bar{w}_k = (Q_k)^{-1/2}w_k$, $\bar{v}_k = (R_k)^{-1/2}v_k$, and $s_k = x_k - \hat{x}_k$. By subtracting Equation (19) from Equation (18), we obtain the following linearised residual observer function at kth time:

$$\begin{aligned} s_{k+1} &= (F_{l,k} - L_kC_{l,k})s_k + B_{l,k}\bar{w}_k - L_kD_{l,k}\bar{v}_k \\ &\quad + (B_{lf,k} - L_kD_{lf,k})f_k \\ \tilde{z}_k &= C_{l,k}s_k + D_{l,k}\bar{v}_k + D_{lf,k}f_k. \end{aligned} \tag{20}$$

$(C_{l,k}, F_{l,k})$ and $(F_{l,k}, B_{l,k})$ are uniformly detectable and stabilisable, respectively, in Equation (18). Assuming that the residual covariance in Equation (18) is convergent, the linearisation compensations in $\bar{w}_k$ and $\bar{v}_k$ are also convergent. Therefore, $E(s_{k+1}s_{k+1}^{\mathrm{T}})$ satisfies the mean square stability.

Considering that Equation (20) is an LDTV system, the solutions of L_k and W_k presented in Julier et al. (2000) can be used to solve Equation (8) approximately as follows:

$$\begin{aligned} L_k &= F_{l,k}P_{k|k-1}(C_{l,k})^{\mathrm{T}}R_{\tilde{y},k}^{-1} \\ &= F_{l,k}P_{k|k-1}^{xx}(P_{k|k-1}^{zz})^{-1} \\ R_{\tilde{y},k} &= C_{l,k}P_{k|k-1}(C_{l,k})^{\mathrm{T}} + D_{l,k}R_k \\ W_k &= (R_{\tilde{y},k})^{-1/2} \\ P_{k+1} &= (I - L_kC_{l,k})P_k(I - L_kC_{l,k})^{\mathrm{T}} + D_{l,k}R_kD_{l,k}^{\mathrm{T}} \end{aligned} \tag{21}$$

The proof of optimality for the linear case is presented next.

First, we define $\Phi(i,j) = \prod_{k=i}^{j-1}(F_{l,k} - L_kC_{l,k})$, $\Phi(i,i) = I$. Further, Equation (20) can be rewritten as

$$\begin{aligned} \tilde{z}_k &= \Omega s_0 + \Gamma_w\bar{w}_N + \Gamma_v\bar{v}_N + \Gamma_f\bar{f}_N \\ r_N &= W_N\tilde{z}_N \end{aligned} \tag{22}$$

where vector υ_N denotes $[\upsilon_0^{\mathrm{T}}, \upsilon_1^{\mathrm{T}} \ldots \upsilon_N^{\mathrm{T}}]^{\mathrm{T}}$ for an arbitrary vector matrix sequence.

$$\Omega = \begin{bmatrix} C_{l,0} \\ C_{l,1}\Phi(1,0) \\ \vdots \\ C_{l,N}\Phi(N,0) \end{bmatrix}$$

For Γ_w,

$$\begin{aligned} \Gamma_\omega &= [\Gamma_\omega(k,j)]_{(N+1)\times(N+1)} \\ \Gamma_\omega(k,k) &= 0, \end{aligned}$$

https://doi.org/10.1017/S0373463322000078 Published online by Cambridge University Press

$$\Gamma_\omega(k,j) = \begin{cases} 0 & \text{for } k < j \\ C_{l,k}\Phi(k-1,j)[B_{l,k},0] & \text{for } k > j \end{cases},$$

$$\Gamma_\omega = [\Gamma_\omega(k,j)]_{(N+1)\times(N+1)}.$$

For Γ_v,

$$\Gamma_\omega = [\Gamma_\omega(k,j)]_{(N+1)\times(N+1)},$$

$$\Gamma_v(k,k) = D_{l,k},$$

$$\Gamma_v(k,j) = \begin{cases} 0 & \text{for } k < j \\ C_{l,k}\Phi(k-1,j)[-L_k D_{l,k}, D_{l,k}] & \text{for } k > j \end{cases}.$$

For Γ_f,

$$\Gamma_f = [\Gamma_f(k,j)]_{(N+1)\times(N+1)},$$

$$\Gamma_f(j,k) = D_{lf,k-1},$$

$$\Gamma_\omega(k,j) = \begin{cases} 0 & \text{for } k < j \\ C_{l,k}\Phi(k-1,j)[B_{lf,k-1} - L_{k-1}D_{lf,k-1}, D_{lf,j}] & \text{for } k > j \end{cases}$$

Then, one can show that

$$||G_{rd}||^2_{\infty,[0,N]} = ||W_N[\Omega P_0^{1/2}, \Gamma_w, \Gamma_v]||_2^2.$$

When no fault exists, Equation (20) is expressed as follows:

$$\begin{aligned} s_{k+1} &= (F_{l,k} - L_k C_{l,k})s_k + B_{l,k}\bar{w}_k - D_{l,k}L_k\bar{v}_k \\ \tilde{z}_k &= C_{l,k}s_k + D_{l,k}\bar{v}_k \end{aligned}$$

where s_0, $\bar{w}_k$ and $\bar{v}_k$ are assumed to be zero-mean Gaussian white noise. L_k, as defined in Equation (21), is the product solution of the well-known gain of KF, i.e., K_k and $F_{l,k}$ (Zhong et al., 2020).

Moreover, the orthogonality of the innovation sequence yields

$$\begin{aligned} E(\tilde{z}_k, \tilde{z}_k^{\mathrm{T}}) &= \mathrm{diag}(R_{\tilde{y},0}, R_{\tilde{y},1}, \ldots, R_{\tilde{y},N}) \\ &= [\Omega,\Gamma_w,\Gamma_v\,]I[\Omega,\Gamma_w,\Gamma_v]^{\mathrm{T}} \\ &= \Omega\Omega^{\mathrm{T}} + \Gamma_w(\Gamma_w)^{\mathrm{T}} + \Gamma_v(\Gamma_v)^{\mathrm{T}}. \end{aligned} \tag{23}$$

Let $\Lambda_k = (F_{l,k} - L_k C_{l,k})P_k C_{l,k}^{\mathrm{T}} + \bar{w}_k - L_k\bar{v}_k$, considering L_k and W_k. We have $\Lambda_k = 0$. When $k \neq j$, all the nondiagonal terms of $H_{rd,k}$ in (9) are equal to $\Lambda_k^{\mathrm{T}} P_k \Phi_{k,j+1}^{\mathrm{T}} C_{l,l}^{\mathrm{T}} = 0$.

Then, when W_k defined in Equation (21) is applied, we obtain

$$\begin{aligned} &W_k(\Omega\Omega^{\mathrm{T}} + \Gamma_w(\Gamma_w)^{\mathrm{T}} + \Gamma_v(\Gamma_v)^{\mathrm{T}})W_k^{\mathrm{T}} \\ &\quad = W_k(\mathrm{diag}(R_{\tilde{y},0}, R_{\tilde{y},1}, \ldots, R_{\tilde{y},N}))W_k^{\mathrm{T}}. \\ &\quad = I \end{aligned} \tag{24}$$

Next, for W_k and L_k, as defined in Equation (21), $||G_{rf}||^2_{\infty,[0,N]} = I$.

Further, according to Zhong et al. (2016), L_k and W_k can be replaced by arbitrary L_{ak} and W_{ak}, for which the FDF remains stable. Thus, there exists a mapping such that the new residual r_{aN} can be recovered from the optimal residual r_N with $r_{aN} = M_{aN}r_N$, where M_{aN} is the mapping matrix.

https://doi.org/10.1017/S0373463322000078 Published online by Cambridge University Press

There exists a mapping (Zhong et al., 2019) $\tilde{z}_{ak} \rightarrow z_{ak}$ such that

$$\begin{aligned} \eta_{k+1} &= (F_{l,k} - L_k C_{l,k})\eta_k + (L_{ak} - L_k)\tilde{z}_{ak} \\ \tilde{z}_k &= C_{l,k}\eta_k + \tilde{z}_{ak}. \end{aligned} \tag{25}$$

The postfilter is set as $W_k = W_{ak}$, and we obtain

$$r_{aN} = W_{aN}\tilde{z}_{aN} = W_{aN}M_{aN}\tilde{z}_N = W_{aN}M_{aN}W_N^{-1}r_N,$$

where matrix M_{aN} is obtained by replacing $B_{lf,k}$, $D_{lf,j}$, and L_k in Γ_f with L_k, I and L_{ak}, respectively.

Let $M_{WN} = W_{aN}M_{aN}W_N^{-1}$. Then, Equation (8) can be rewritten as follows:

$$\begin{aligned} \frac{||G_{rf}||^2_{\infty,[0,N]}}{||G_{rd}||^2_{\infty,[0,N]}} &= \frac{||M_{WN}G_{rf}||^2_{\infty,[0,N]}}{||M_{WN}G_{rd}||^2_{\infty,[0,N]}} \\ &= \frac{||M_{WN}G_{rf}||^2_{\infty,[0,N]}}{||M_{WN}||^2_{\infty,[0,N]}} \leq \frac{||M_{WN}||^2_{\infty,[0,N]}||G_{rf}||^2_{\infty,[0,N]}}{||M_{WN}||^2_{\infty,[0,N]}} \\ &= ||G_{rf}||^2_{\infty,[0,N]} \end{aligned}$$

Alternatively,

$$\begin{aligned} \frac{||G_{rf}||^2_{-,[0,N]}}{||G_{rd}||^2_{\infty,[0,N]}} &= \frac{||M_{WN}G_{rf}||^2_{-,[0,N]}}{||M_{WN}G_{rd}||^2_{\infty,[0,N]}} \\ &= \frac{||M_{WN}G_{rf}||^2_{-,[0,N]}}{||M_{WN}||^2_{\infty,[0,N]}} \leq \frac{||M_{WN}||^2_{\infty,[0,N]}||G_{rf}||^2_{-,[0,N]}}{||M_{WN}||^2_{\infty,[0,N]}} \\ &= ||G_{rf}||^2_{-,[0,N]} \end{aligned}$$

Thus, W_k and L_k proposed in Equation (21) provide an optimal solution to Equation (8).

Remark 2: P_{k+1} in Equation (21) is the solution obtained by directly substituting L_k into KF covariance based on the framework of the least-squares estimation. When parameters are designed in this manner, the accuracy of state estimation is compromised and the FD performance is improved by ensuring the stability of the filter framework.

Remark 3: Note that a large $||G_{rf}||^2_{\infty,[0,N]}$ does not lead to residual sensitivity to faults. However, we still adopt a large $||G_{rf}||^2_{\infty,[0,N]}$ because it has been widely reported in the literature and because it has the same optimal solution to the H_i/H_∞ problem.

3.2. Randomised analysis of FAR

The choice of $J_{th,0}$ in Equation (12) determines the performance of FD. However, a tradeoff between the FAR and fault diagnosis accuracy is required. The smaller the $J_{th,0}$, the better is the fault diagnosis accuracy but the poorer is the FAR.

Let us consider the irregular influence of environmental temperature, variation and electromagnetic interference on the inertial measurement unit and the instability of the GNSS signal when ships sail at sea. δ_d in Equation (12) and the probability density function are usually unknown. Thus, a randomised algorithm for probabilistic analysis (Zhong et al., 2016, 2019) is necessary to estimate the worst-case threshold for generating an acceptable FAR.

As it is difficult to set the value of the threshold δ_d in Equation (12), it can be solved to obtain the sample bounds for estimating the extremum of a random variable as proposed in Chapter 8.4 of Tempo et al. (2012). First, the number M of the samples in the fault-free case ($f_k = 0$) are set and a probabilistic

https://doi.org/10.1017/S0373463322000078 Published online by Cambridge University Press

estimate of the worst-case performance is obtained as follows:

$$\hat{J}_N = \max_i J_N^{(i)}. \tag{26}$$

In a system without faults, M depends on the number of sampling points. Then, $\alpha, \beta \in (0, 1)$ if the following sample bound is satisfied under the worst-case performance condition:

$$M \geq \frac{\lg \beta}{\lg(1-\alpha)}. \tag{27}$$

$\hat{J}_N$ returns a probabilistic estimation of the threshold generating a given FAR with confidence level $1-\beta$. The probability P_{FAR} of the FD rate is obtained as

$$P_{\mathrm{FAR}} = \Pr\{J_N > J_{th} | f_k = 0\} < \alpha \tag{28}$$

The entire cubature H_i/H_∞-FDF with a given FAR can be obtained as follows:

Step 1. Set sampling time N, $k = 0$, and set the initial state $x_0 = 0$.
Step 2. Calculate L_k and W_k using Equation (21).
Step 3. Calculate z_{k+1} using Equation (4).
Step 4. Update $\hat{x}_{k+1}$ and r_{k+1} using Equation (19).
Step 5. Reset $\hat{x}_{k+1} = 0$.
Step 6. Calculate J_N using Equation (12).
Step 7. Choose a threshold using Equation (26), and detect the fault.
Step 8. $k = k + 1$, return to step 2.

4. Experimental results and discussion

4.1. Description of the simulation scheme

First, to demonstrate the effectiveness of the proposed method, a manoeuvring model group (MMG) model was used whose physical meaning can be clearly interpreted, as proposed by Ogawa and Kasai (1978). Using this model, sensor data during motion in multiple experiments were generated. The main feature of MMG modelling is that the hydrodynamic forces and moments are clearly decomposed into those acting on the hull, propeller and rudder and those of the interaction among them. Although ship dynamic models have been developed by many scholars (Fossen, 2011; Liang and Jia, 2015), the state estimation accuracy of integrated navigation algorithm is thought to be mainly affected by the initial-state estimation error in the sensor, the system process noise and the measurement noise. This paper proposes an original MMG model that reflects the law of ship motions, which can be refined into a more complex ship dynamic model in future. Based on this classification, the differential equations for velocity, attitude, angular rate and displacement for a vessel's linear and rotation movements around the X-, Y- and Z-axis in the body frame can be solved using Newton's laws. Then, the obtained states are inversed according to the principle of mechanical arrangement and the noise characteristics of the sensors (Table 1). Thus, the simulated sensor data can be obtained, as shown in Figure 1. The interfaces of the simulation system are shown in Figure 2. Because pitching and heaving are not the key considerations for surface merchant vessels, these states were excluded. To avoid accidental conclusions, each experiment was repeated 20 times and the values of simulated sensor noise and the results of integrated navigation were averaged.

The process and measurement noises are modelled as first-order Markov process according to the IEEE standards of 2003 and 2016. Second, many factors may cause the failure of the loosely coupled SINS/GNSS integrated navigation system. To summarise, the faults can be divided into hard and soft faults. Hard faults are caused by the sudden faults of measurement output, while soft faults are caused by slow changes due to faults over time.

https://doi.org/10.1017/S0373463322000078 Published online by Cambridge University Press

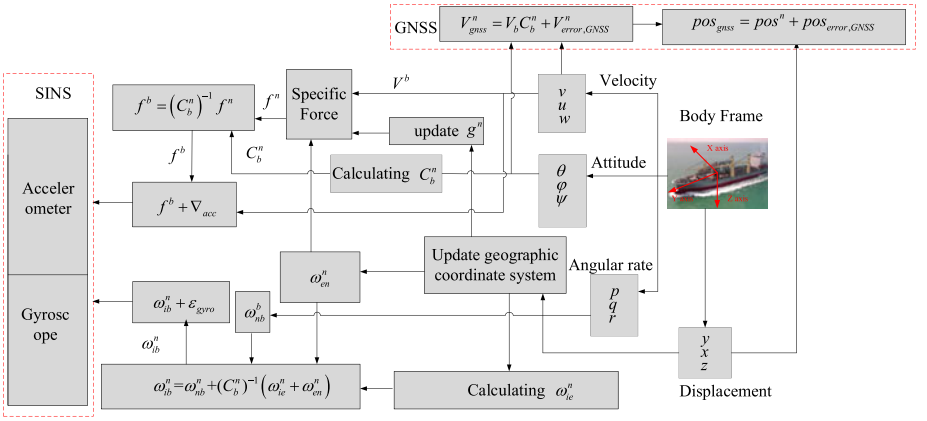


Figure 1. *Process of simulation of surface ship sensor data generation.*

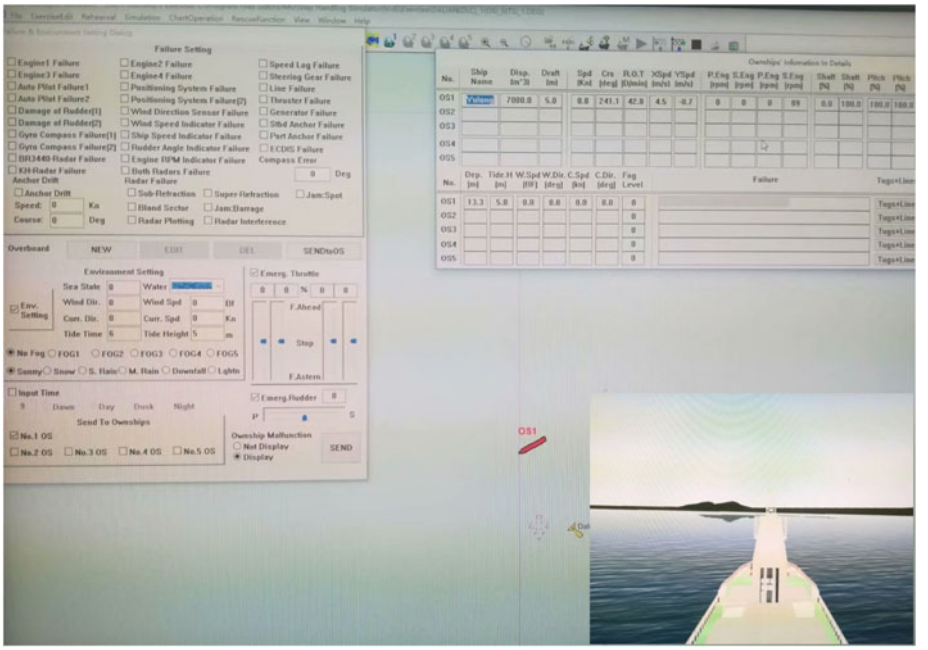


Figure 2. *Interfaces for setting the ship parameters and ship manoeuvring.*

Table 1. *Detailed parameters of the SINS (MTi-G-710 produced by XSENS)/GNSS generated by the simulator.*

		Values		
Sensors		Bias	Noise density	Run bias density
SINS (200 Hz)	Gyrocompass	0·20 °/s	0·01 °/s/$\sqrt{\text{Hz}}$	10·0 °/h
	Accelerometer	5 mg	60 μg/$\sqrt{\text{Hz}}$	15 μg
GNSS (1 Hz)	Position error	6 m		
	Velocity error	0·6 m/s		

https://doi.org/10.1017/S0373463322000078 Published online by Cambridge University Press

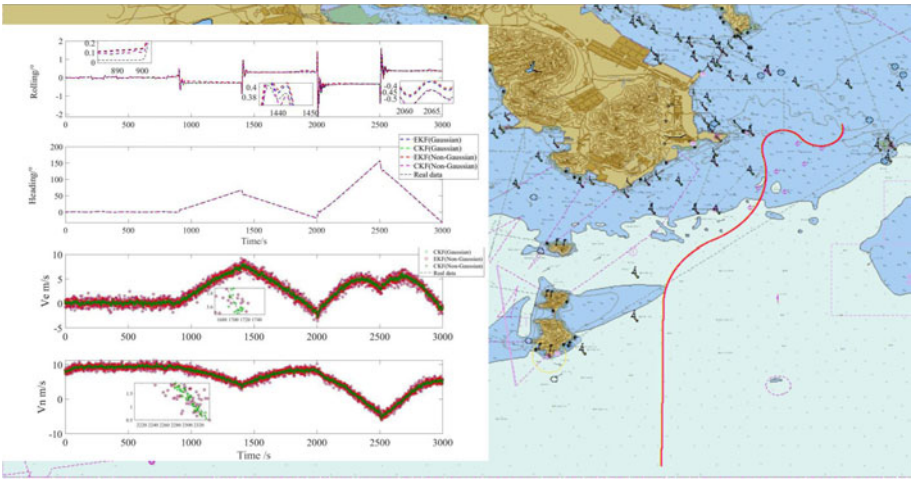


Figure 3. *Trajectory and motion states of the simulation experiment.*

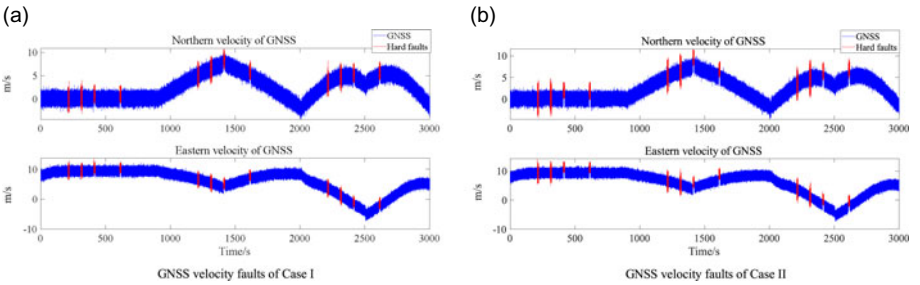


Figure 4. *GNSS velocity measurement values after adding hard faults. (a) GNSS velocity faults of case I. (b) GNSS velocity faults of case II.*

Hard faults (Zhang et al., 2020) can be expressed as follows:

$$y = \begin{cases} \text{count } (t_1 < t < t_2) \\ 0 \ (t \geq t_2 \text{ or } t \leq t_1) \end{cases}. \tag{29}$$

Soft faults can be expressed as follows:

$$y = k(t - t_1)^n + b, \tag{30}$$

where t is the time, y is the fault value, k is the fault coefficient, t_1 and t_2 are the start and end times of the fault, respectively, and *count* is the fault information when faults occur.

In the SINS/GNSS system, the main GNSS fault is a short-term outage caused by factors such as interference and signal masking. Thus, for GNSS intermittent faults, we should impose strict requirements for detecting hard faults under different motions. Meanwhile, the SINS on a surface vessel is easily affected by environmental temperature, violent motion variation and electromagnetic interference, which will lead to state divergence as errors accumulate over time. Thus, soft faults mainly affect the performance of SINS.

https://doi.org/10.1017/S0373463322000078 Published online by Cambridge University Press

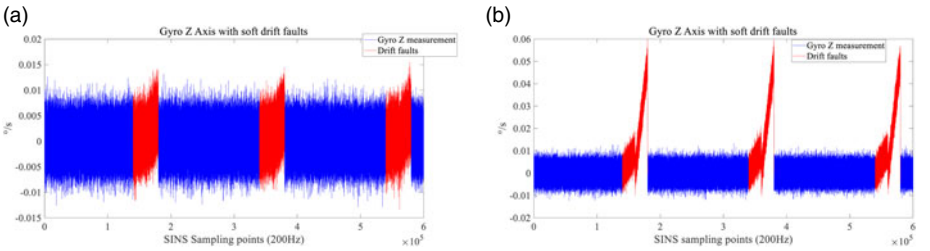


Figure 5. *Simulated soft drift faults in the gyro Z-axis of the SINS system. (a) SINS faults of case I. (b) SINS faults of case II.*

Table 2. *Simulated hard and soft faults added into the SINS/GNSS system.*

No.	Time	Simulated faults case I	Simulated faults case II
1	110 s < t < 120 s, 1110 s < t < 1120 s, 2110 s < t < 2120 s	$\delta P_{\mathrm{GNSS}} = 1.5 * \delta P_{\mathrm{GNSS}}$	or $\delta P_{\mathrm{GNSS}} = 2 * \delta P_{\mathrm{GNSS}}$
2	210 s < t < 220 s, 1210 s < t < 1220 s, 2210 s < t < 2220 s	$\delta V_{\mathrm{GNSS}} = 1.5 * \delta V_{\mathrm{GNSS}}$	or $\delta V_{\mathrm{GNSS}} = 2 * \delta V_{\mathrm{GNSS}}$
3	310 s < t < 320 s, 1310 s < t < 1320 s, 2310 s < t < 2320 s	$\delta V_{\mathrm{GNSS}} = 1.5 * \delta V_{\mathrm{GNSS}}$	or $\delta P_{\mathrm{GNSS}} = 1.5 * \delta P_{\mathrm{GNSS}}$
4	410 s < t < 420 s, 1410 s < t < 1420 s, 2410 s < t < 2420 s	$\delta V_{\mathrm{GNSS}} = \delta V_{\mathrm{GNSS}} + 1$ (m/s)	or $\delta V_{\mathrm{GNSS}} = \delta V_{\mathrm{GNSS}} + 2$(m/s)
5	510 s < t < 520 s, 1510 s < t < 1520 s, 2510 s < t < 2520 s	$\delta P_{\mathrm{GNSS}} = \delta P_{\mathrm{GNSS}} + 3$(m)	or $\delta P_{\mathrm{GNSS}} = \delta P_{\mathrm{GNSS}} + 6$ (m)
6	610 s < t < 620 s, 1610 s < t < 1620 s, 2610 s < t < 2620 s	$\delta P_{\mathrm{GNSS}} = \delta P_{\mathrm{GNSS}} + 3$(m) $\delta V_{\mathrm{GNSS}} = \delta V_{\mathrm{GNSS}} + 1$(m/s)	or $\delta P_{\mathrm{GNSS}} = \delta P_{\mathrm{GNSS}} + 6$(m) $\delta V_{\mathrm{GNSS}} = \delta V_{\mathrm{GNSS}} + 2$(m/s)
7	700 s < t < 800 s, 1700s < t < 1800s, 2700 s < t < 2800 s	$w_k = w_k + (0.036°/\mathrm{h}) * t$	$w_k = w_k + (0.36°/\mathrm{h}) * t$
8	800 s < t < 900 s, 1800s < t < 1900s, 2800 s < t < 2900 s	$w_k = w_k + (0.18°/\mathrm{h}) * t$	$w_k = w_k + (1.8°/\mathrm{h}) * t$

4.2. Simulation study and discussion

To verify the effectiveness of the proposed FD algorithm, the simulated data in Table 1 and a set of $l_2[0, N]$-norm-bounded ω_k and v_k were used. Further, $C_b^n \Delta w_k$ and Δv_k were added to the simulated SINS and GNSS noise with a non-Gaussian distribution in a complex environment. Then, the simulated faults were added for various cases.

$$\Delta w_k = [0.018°/\mathrm{h}, 0.018°/\mathrm{h}, 0.018°/\mathrm{h}, 1\ \mu\mathrm{g}, 1\ \mu\mathrm{g}, 1\ \mu\mathrm{g}]^{\mathrm{T}} \sin 2\pi t,$$
$$\Delta v_k = [0.1, 0.1, 0.1, 1e^{-8}, 1e^{-8}, 1]^{\mathrm{T}} \sin 2\pi t.$$

Next, various faults were added when the ship followed different trajectories with different motions (e.g., linear motion and alteration of course and turning) under wind and wave disturbances. Data from a normal navigation simulation were employed. The trajectory and motion state measured using different integrated navigation methods with faults in sensors are shown in Figure 3. The GPS outlier (hard faults) and unexpected inertial sensor drift (soft faults) are considered faults (Table 2). For comparison, the same faults in all three motion modes were added. In addition, the velocity faults of GNSS and the simulated soft drift faults in the Gyro Z-axis of SINS system are shown in Figures 4 and 5.

https://doi.org/10.1017/S0373463322000078 Published online by Cambridge University Press

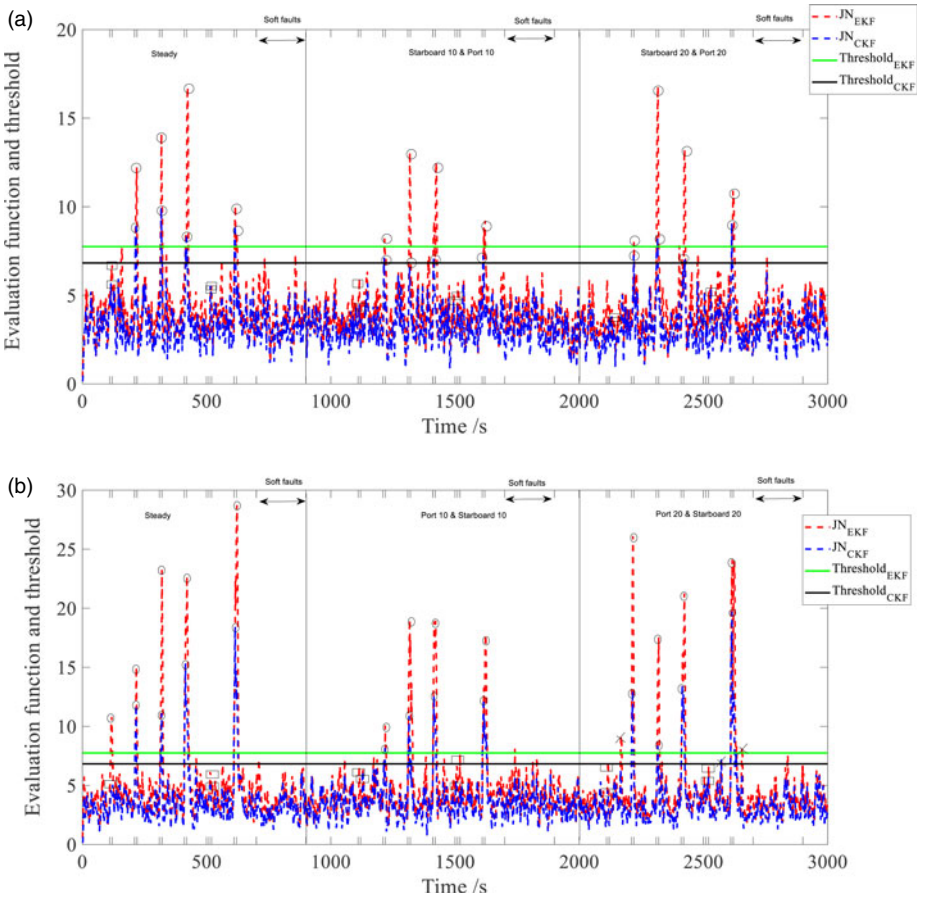


Figure 6. *Simulated H_i/H_∞ FDF results of case I faults listed in Table 2. (a) simulated faults with small GNSS error in case I of Table 2. (b) simulated faults with large GNSS error in case I of Table 2.*

The trajectory and the motion states are shown in Figure 3. Regardless of whether the system noise and measurement noise are zero-mean Gaussian white noise, the velocity estimation performance of EKF is worse than that of CKF when there are faults in the sensors. With regard to attitude estimation, the difference between the estimation accuracies of EKF and CKF is not obvious when the ship is steady. However, for EKF, with an increasing alteration of the course, the faults cause attitude estimation divergence, especially when the ship turns sharply. (The performance of the case with non-zero-mean Gaussian white noise is worse than that of the case with zero-mean Gaussian white noise.) In other words, although the velocity and position of the GNSS are observable, the EKF can be used to estimate the attitude error in theory to correct the attitude divergence of SINS. However, this correction cannot compensate for the degradation in navigation accuracy caused by sensor faults. An accurate estimation of the velocity and position of the integrated navigation system based on only EKF shows that such a system is considerably dependent on the measurement accuracy of the GNSS. The measurement accuracy of a system based on EKF is worse than that of a system based on CKF when sensor faults are present and when the vessels sailing on the seas perform sharp course alteration or turning manoeuvres.

Next, the threshold is analysed. $J_N >$ Threshold implies that the FDF detects the faults. FAR is equal to zero in the fault-free case, and according to Equation (26), we have $\hat{J}_N = \max_i J^{(i)}_{N,(\text{Cubature})} = 7.3173$ and $\hat{J}_N = \max_i J^{(i)}_{N,(\text{Extended})} = 8.5421$ with a sliding window set with $N = 5$ in Equation (18). However, generally, both the threshold of δ_d in Equation (18) and the probabilistic density function are unknown

https://doi.org/10.1017/S0373463322000078 Published online by Cambridge University Press

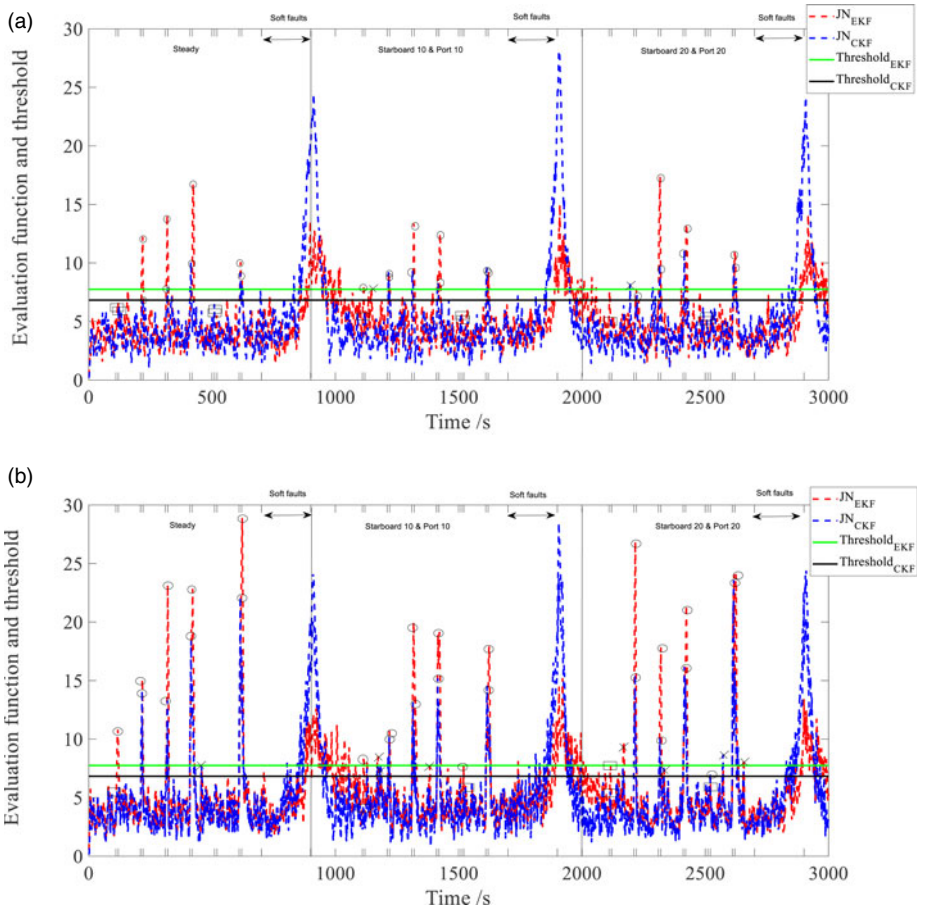


Figure 7. *Simulated H_i/H_∞ FDF results of case II faults in Table 2. (a) Simulated faults with small GNSS error in case II of Table 2. (b) Simulated faults with large GNSS in case II of Table 2.*

in practice; hence, the theory in Section 3.2 can be used. Setting the sampling time $M = 3000$ in Equation (27), we obtain an acceptable FAR $= 1 - \alpha = 0.999$, from which β is obtained by solving $3000 \geq \lg\beta/(\lg(1-\alpha))$. We thus obtain $\beta = 0.0023$. The FAR probability with $\text{Threshold}_{\text{EKF}} = 7.7941$ and $\text{Threshold}_{\text{CKF}} = 6.8226$ are less than 0·999 with a confidence level of 0·9977. The FD results based on extended H_i/H_∞ FDF (Zhong et al., 2016) and cubature H_i/H_∞ FDF are shown in Figures 6 and 7. The circles, boxes and crosses in the figures represent successful detections, false positives and false negatives respectively, excluding SINS soft faults.

Figure 6 plots the FD results of Case I using the extended H_i/H_∞ FDF and cubature H_i/H_∞ FDF. When the SINS faults were small, neither the extended H_i/H_∞ FDF nor the cubature H_i/H_∞ FDF effectively detected the soft SINS faults of the system [Figure 6(a)] and small GNSS faults are added on the system. The extended H_i/H_∞ FDF and cubature H_i/H_∞ FDF both gave six false negatives, which were mainly position faults with small difference when converted into longitude and latitude. Moreover, the extended H_i/H_∞ FDF was more sensitive to fault responses than the cubature H_i/H_∞ FDF, as reflected in the larger evaluation function threshold value. When larger GNSS faults were added to the GNSS, the evaluation function thresholds of both the extended and cubature H_i/H_∞ FDFs become larger than those in Case I. The extended H_i/H_∞ FDF yielded four false positives and three false negatives, whereas the cubature H_i/H_∞ FDF obtained six false positives and one false negative. Besides being more sensitive to faults, the extended H_i/H_∞ FDF had increased false positive rate. The abovementioned simulation shows that

https://doi.org/10.1017/S0373463322000078 Published online by Cambridge University Press

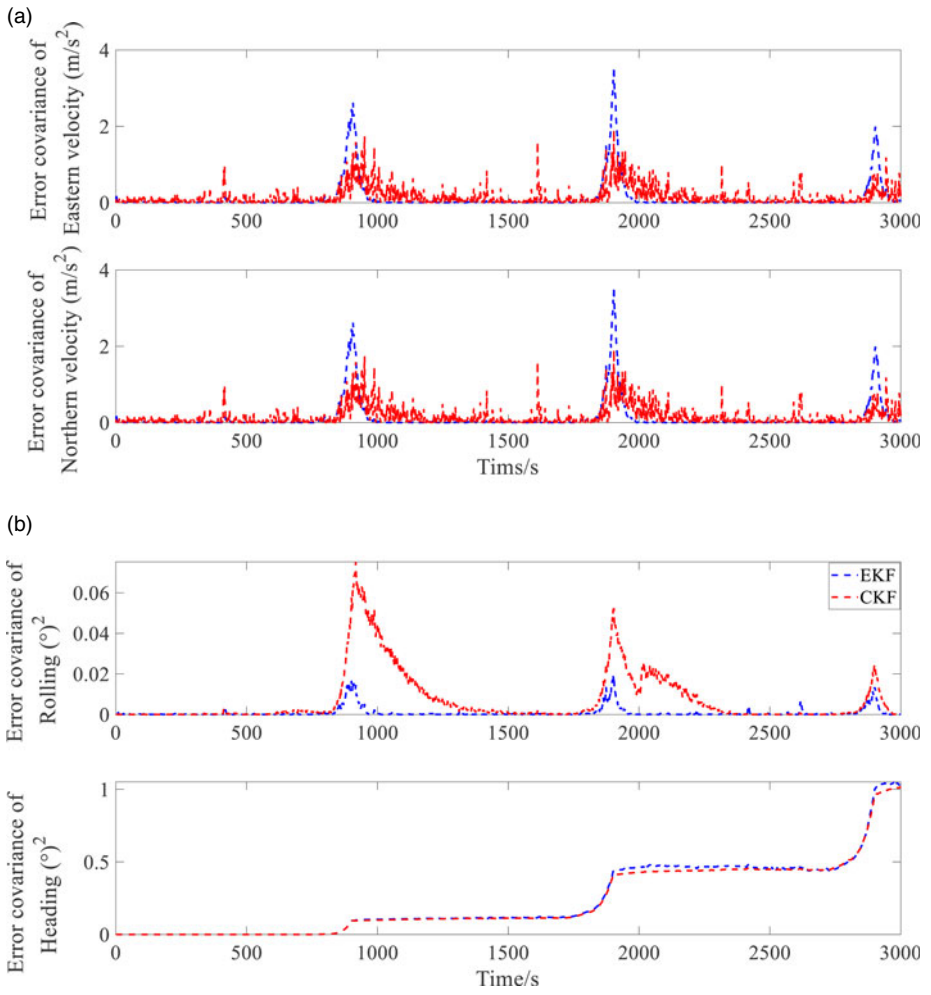


Figure 8. *Simulated state estimation covariance with small GNSS faults in case I. (a) Simulated velocity estimation covariance with small GNSS faults in case I. (b) Simulated attitude estimation covariance with small GNSS faults in case I.*

both the methods can effectively detect hard faults of GNSS, but are not sufficiently sensitive to soft, low-magnitude faults of SINS.

Figure 7 shows the simulation results in the case of larger SINS faults. The detection results of hard faults were similar to those in case I. Soft faults occurred between 700 and 900 s, 1,700 and 1,900,s, and 2,700 and 2,900s. After the soft faults disappear, the detection results of the extended H_i/H_∞ FDF included many false alarms, especially in the linear motion stage during 700s~900 s. In the turning phase, however, the number of FD false negatives based on extended H_i/H_∞ FDF has decreased. The cubature H_i/H_∞ FDF converged at faster speed and gave fewer false alarms after the end of soft faults than the extended H_i/H_∞ FDF and completed the detection of hard faults. These results confirm the effectiveness of the proposed algorithm.

When the soft drift faults of SINS are too small, they cannot be detected by the H_i/H_∞ FDF algorithm in every motion stage. The integrated navigation algorithm based on CKF achieves high state estimation accuracy. However, when a soft fault occurs, the amplitude of the J_N change is not obvious. However, the error covariance of the state changes significantly (Figure 8). This behaviour will be studied in the

https://doi.org/10.1017/S0373463322000078 Published online by Cambridge University Press

authors' future work. The FD relies not only on the observations but also on the attitude covariance in P_k of Equation (21) to determine the presence of soft drift faults.

5. Conclusions

The H_i/H_∞ optimised FD of commonly hard intermittent faults and continuous soft drift faults for a low-cost loosely coupled SINS/GNSS integrated navigation system for a surface vessel were investigated in a CKF frame. To compensate for the modelling error, energy-bounded disturbances and noise while simultaneously considering both the robustness to disturbance and the sensitivity to fault, a cubature H_i/H_∞ FDF with a threshold considering a randomised FAR is proposed. Finally, a simulator based on ship manoeuvring with faults in different motion states is used to examine the performance of the cubature H_i/H_∞ FDF and that of an extended H_i/H_∞ FDF for comparison. For the extended H_i/H_∞ FDF, in the presence of interference by an unknown noise, the characteristics of the unknown noise and soft drift faults affect the system for a certain period of time, resulting in errors in state estimation and rendering the advantages of the integrated navigation system and FD insignificant. The measurement fault detection performance of cubature H_i/H_∞ FDF is similar to that of the extended H_i/H_∞ FDF. When the system noise is large, the cubature H_i/H_∞ FDF outperforms the extended H_i/H_∞ FDF for fault detection and provides a more stable state estimation. Moreover, to detect soft drift faults more accurately, the state-error covariance matrix will be considered in future work.

Funding. This work was supported by the National Nature Science Foundation of China (Nos. 51579024, 51879027, 61374114) and the Fundamental Research Funds for the Central Universities (DMU no. 3132016311).

References

Chiang, K. W., Tsai, G. J., Li, Y. H., Li, Y. and El-Sheimy, N. (2020). Navigation engine design for automated driving using INS/GNSS/3d LiDAR-SLAM and integrity assessment. *Remote Sensing*, **12**(10), 1564.

Fossen, T. I. (2011). *Handbook of Marine Craft Hydrodynamics and Motion Control*. Hoboken, NJ, USA: Wiley.

Gao, G., Gao, S., Hong, G., Peng, X. and Yu, T. (2020). A robust INS/SRS/CNS integrated navigation system with the Chi-square test-based robust Kalman filter. *Sensors*, **20**(20), 5909.

Guo, D., Zhong, M., Ji, H., Liu, Y. and Yang, R. (2018). A hybrid feature model and deep learning based fault diagnosis for unmanned aerial vehicle sensors. *Neurocomputing*, **319**, 155–163.

Guo, C., Li, F., Tian, Z., Guo, W. and Tan, S. (2020). Intelligent active fault-tolerant system for multi-source integrated navigation system based on deep neural network. *Neural Computing and Applications*, **32**(22), 16857–16874.

IEEE. (2008). IEEE 952-1997 - IEEE Standard Specification Format Guide and Test Procedure for Single-Axis Interferometric Fiber Optic Gyros, 24 February 2003, in IEEE STD, 38–84. Institute of Electrical and Electronics Engineers.

IMO (2009). International Maritime Organization. International Convention for Safety of Life at Sea (SOLAS). Chapter V, pp. 262–296.

Jiang, W., Liu, D., Cai, B., Rizos, C., Wang, J. and Shangguan, W. (2019). A fault-tolerant tightly coupled GNSS/INS/OVS integration vehicle navigation system based on an FDP algorithm. *IEEE Transactions on Vehicular Technology*, **68**(7), 6365–6378.

Julier, S., Uhlmann, J. and Durrant-Whyte, H. F. (2000). A new method for the nonlinear transformation of means and covariances in filters and estimators. *IEEE Transactions on Automatic Control*, **47**(8), 1406–1409.

Khan, A. Q., Abid, M. and Ding, S. X. (2014). Fault detection filter design for discrete-time nonlinear systems – A mixed optimization. *Systems & Control Letters*, **67**, 46–54.

Li, X. and Zhou, K. (2009). A time domain approach to robust fault detection of linear time-varying systems. *Automatica*, **45**(1), 94–102.

Li, Y., Hou, L., Yang, Y. and Tong, J. (2020). Huber's M-estimation-based cubature Kalman filter for an INS/DVL integrated system. *Mathematical Problems in Engineering*, **2020**.

Liang, Y. and Jia, Y. (2015). A nonlinear quaternion-based fault-tolerant SINS/GNSS integrated navigation method for autonomous UAVs. *Aerospace Science and Technology*, **40**, 191–199.

Liu, H., Zhong, M. and Yang, R. (2018). Simultaneous disturbance compensation and H_i/H_∞ optimization in fault detection of UAVs. *International Journal of Applied Mathematics and Computer Science*, **28**(2), 349–362.

Liu, H., Zhong, M. and Liu, Y. (2019a). A new residual evaluation function based fault diagnosis for a kind of nonlinear systems. *Asian Journal of Control*, **21**(3), 1153–1165.

Xiong, Y., Huang, H., Guo, X., Zhang, Y. and Shen, C. (2019b). Combination of iterated cubature Kalman filter and neural networks for GPS/INS during GPS outages. *Review of Scientific Instruments*, **90**(12), 125005.

https://doi.org/10.1017/S0373463322000078 Published online by Cambridge University Press

Liu, D., Wang, H, Xia, Q and Jiang, C (2020). A low-cost method of improving the GNSS/SINS integrated navigation system using multiple receivers. *Electron*, **9**(7), 1079.

Liu, W., Liu, Y., Gunawan, B. A. and Bucknall, R. (2021). Practical moving target detection in maritime environments using fuzzy multi-sensor data fusion. *International Journal of Fuzzy Systems*, 1–9.

Majidi, M., Erfanian, A. and Khaloozadeh, H. (2020). Prediction-discrepancy based on innovative particle filter for estimating UAV true position in the presence of the GPS spoofing attacks. *IET Radar, Sonar and Navigation*, **14**(6), 887–897.

Ogawa, A. and Kasai, H. (1978). On the mathematical method of manoeuvring motion of ships. *International Shipbuilding Progress*, **25**(292), 306–319.

Qin, H., Wu, Z., Sun, Y. and Chen, H. (2019). Disturbance-observer-based prescribed performance fault-tolerant trajectory tracking control for ocean bottom flying node. *IEEE Access*, **7**, 49004–49013.

Song, R., Chen, X., Fang, Y. and Huang, H. (2020). Integrated navigation of GPS/INS based on fusion of recursive maximum likelihood IMM and square-root cubature Kalman filter. *ISA Transactions*, **105**, 387–395.

Tempo, R., Calafiore, G. and Dabbene, F. (2012). *Randomized Algorithms for Analysis and Control of Uncertain Systems: With Applications*. London: Springer Science+Business Media.

Wang, N. and Karimi, H. R. (2020). Successive waypoints tracking of an underactuated surface vehicle. *IEEE Transactions on Industrial Informatics*, **16**(2), 898–908.

Wang, J. L., Yang, G.-H. and Liu, J. (2007). An LMI approach to H-index and mixed H_-/H_∞ fault detection observer design. *Automatica*, **43**(9), 1656–1665.

Wang, N., Karimi, H. R., Li, H. and Su, S. F. (2019). Accurate trajectory tracking of disturbed surface vehicles: A finite-time control approach. *IEEE/ASME Transactions on Mechatronics*, **24**(3), 1064–1074.

Wen, Z., Yan, G., Cai, Q. and Sun, Y. (2019). Odometer aided SINS in-motion alignment method based on backtracking scheme for large misalignment angles. *IEEE Access*, **8**, 7937–7948.

Xiong, H., Bian, R., Li, Y., Du, Z. and Mai, Z. (2020). Fault-tolerant GNSS/SINS/DVL/CNS integrated navigation and positioning mechanism based on adaptive information sharing factors. *IEEE Systems Journal*, **14**(3), 3744–3754.

Xu, H. and Lian, B. (2018). Fault detection for multi-source integrated navigation system using fully convolutional neural network. *IET Radar, Sonar and Navigation*, **12**(7), 774–782.

Zhang, C., Zhao, X., Pang, C., Wang, Y., Zhang, L. and Feng, B. (2020). Improved fault detection method based on robust estimation and sliding window test for INS/GNSS integration. *The Journal of Navigation*, **73**(4), 776–796.

Zhao, J. and Mili, L. (2019). A theoretical framework of robust H-infinity unscented Kalman filter and its application to power system dynamic state estimation. *IEEE Transactions on Signal Processing*, **67**(10), 2734–2746.

Zhao, L., Kang, Y., Cheng, J. and Wu, M. (2019). A fault-tolerant polar grid SINS/DVL/USBL integrated navigation algorithm based on the centralized filter and relative position measurement. *Sensors*, **19**(18), 3899.

Zhong, M., Ding, S. X. and Ding, E. L. (2010). Optimal fault detection for linear discrete time-varying systems. *Automatica*, **46**(8), 1395–1400.

Zhong, M., Liu, H. and Song, N. (2015). On designing an extended -FDF for a class of nonlinear systems. *IFAC-PapersOnLine*, **48**(21), 707–712.

Zhong, M., Liu, C., Zhou, D., Li, W. and Xue, T. (2019). Probability analysis of fault diagnosis performance for satellite attitude control systems. *IEEE Transactions on Industrial Informatics*, **15**(11), 5867–5876.

Zhong, M., Guo, J., Guo, D. and Yang, Z. (2016). An extended optimization approach to fault detection of INS/GPS-integrated system. *IEEE Transactions on Instrumentation and Measurement*, **65**(11), 2495–2504.

Zhong, M., Ding, S. X., Zhou, D. and He, X. (2020). An optimization approach to event-triggered fault detection for linear discrete time systems. *IEEE Transactions on Automatic Control*, **65**(10), 4464–4471.

Zhu, Y. and Zhou, L. (2020). A novel approach for fault detection in integrated navigation systems. *IEEE Access*, **8**, 178954–178961.

Cite this article: Guo M, Guo C, Zhang C (2022). H_i/H_∞-optimised fault detection for a surface vessel integrated navigation system. *The Journal of Navigation* **75**: 3, 554–571. https://doi.org/10.1017/S0373463322000078

https://doi.org/10.1017/S0373463322000078 Published online by Cambridge University Press